ChemComm

COMMUNICATION

View Article Online
View Journal | View Issue

Cite this: *Chem. Commun.*, 2025, **61**, 10562

Received 21st May 2025,
Accepted 9th June 2025

DOI: 10.1039/d5cc02883c

rsc.li/chemcomm

Hierarchical ZSM-5 with tunable structure and enhanced mass diffusion†

Xuan Wu,‡[a] Bo-Jun Zeng,‡[a] Si-Ming Wu,‡*[a] Lu Wu,[a] Liang Mao,[a] Yi-Tian Wang,[a] Feng-Juan Wu,[a] Ge Tian,*[a] Li-Ying Wang,[c] Gang-Gang Chang,[a] Christoph Janiak[d] and Xiao-Yu Yang*[ab]

Hierarchical zeolites offer improved mass transfer and catalytic performance, yet their controlled synthesis remains challenging. We report a one-pot synthesis of size-tunable, rod-shaped aligned ZSM-5 (RA-ZSM-5) using tetraethylammonium and tetrabutylammonium hydroxides. The crystallization mechanism and improved mass diffusion associated with the hierarchical structure are elucidated.

Zeolites are widely used as catalysts, adsorbents, desiccants, and ion exchange materials in petroleum processing and the chemical industry.[1–4] However, the inherent microporous structure of zeolites often limits mass transport, which significantly restricts their use in various applications.[5,6] Construction of zeolites with hierarchical structures has been demonstrated as an effective strategy to overcome diffusion limitations in order to extend the lifetime of catalysts.[7–9] There are two main categories of methods for the preparation of hierarchical zeolites:[10,11] *in situ* approaches, in which carbonaceous materials or organic materials serve as templates or seed-induced synthesis is utilized,[12–15] and post-synthesis approaches, which rely on demetallation and/or delamination.[16–19] However, because these methods usually require complex procedures, the range of applications of hierarchical zeolites is limited. In addition, the non-uniform structures of pores in these zeolites, characterized by variations in pore sizes and shapes, cause bottlenecks that limit effective diffusion of reactants and products of processes they promote.[20]

In recent years, one-step processes that produce hierarchical zeolites in a size-controlled manner have been developed.[21–25] For instance, Zhao *et al.* prepared assembled structure type MFI nanocrystals with controlled *b*-axis dimensions by using an *in situ* approach involving two quaternary ammonium salts as structure directing agents (SDAs).[22] Recently, we developed a facile method for this purpose that uses two common structure-directing agents to generate hierarchical ZSM-5 crystals having controllable *a*-axis aligned substructures.[25] Although interest in hierarchical assemblies of zeolites is continuously growing, only a few studies aimed at designing strategies that enable sub-structure size control have been described. Therefore, there is great interest in discovering simple methods for size-controlled synthesis of hierarchical zeolites.

In this work, we developed a one-pot hydrothermal method to construct rod-shaped aligned ZSM-5 zeolite (RA-ZSM-5) using commonly available tetraethylammonium hydroxide (TEAOH) and tetrabutylammonium hydroxide (TBAOH). Moreover, the width of the nanorod can be increased from 40 to 170 nm by increasing the Si/Al molar ratio from 12.5 to 100. Also, the analysis of the evolution of crystal structures and the roles played by the SDAs has provided information about the mechanism responsible for the *c*-axis aligned hierarchical zeolite nanorods. The hierarchical structures enable RA-ZSM-5 zeolite to exhibit enhanced mass diffusion and catalytic stability.

X-ray diffraction (XRD) patterns in Fig. S1 (ESI†) indicate that the typical MFI structure is produced when both TBA^+ and TEA^+ are present in the initial gel. The corresponding SEM images (Fig. S2a, ESI†) suggest that rod-shaped aligned crystals are generated when the TBA^+/TEA^+ molar ratios are below 0.27 : 0.03. Interestingly, the size of nanorods (widths are used to evaluate sizes; Fig. S2b, ESI†) is relatively small when the proportion of TEA^+ is low. The N_2 adsorption–desorption isotherms and corresponding pore size distributions demonstrate

[a] *State Key Laboratory of Advanced Technology for Materials Synthesis and Processing & State Key Laboratory of Silicate Materials for Architectures & School of Chemistry, Chemical Engineering and Life Sciences & School of Materials Science and Engineering & International School of Materials Science and Engineering, Wuhan University of Technology, Wuhan, 430070, China. E-mail: wusiming@whut.edu.cn, tiange@whut.edu.cn, xyyang@whut.edu.cn*

[b] *National Energy Key Laboratory for New Hydrogen-Ammonia Energy Technologies, Foshan Xianhu Laboratory, Foshan, 528200, China*

[c] *State Key Laboratory of Magnetic Resonance and Atomic and Molecular Physics, National Center for Magnetic Resonance in Wuhan, Wuhan Institute of Physics and Mathematics, Innovation Academy for Precision Measurement Science and Technology, Chinese Academy of Sciences, Wuhan, 430071, China*

[d] *Institut für Anorganische Chemie und Strukturchemie, Heinrich-Heine-Universität Düsseldorf, Düsseldorf, 40204, Germany*

† Electronic supplementary information (ESI) available. See DOI: https://doi.org/10.1039/d5cc02883c

‡ These authors contributed equally to this work.

(Fig. S3 and Table S1, ESI†) that RA-ZSM-5 zeolite with TBA^+/TEA^+ = 0.25 : 0.05 has the largest surface area and exhibits a distribution of mesopores. A comparison of the properties of zeolites produced using different temperatures (Fig. S4, ESI†) indicates that the hydrothermal process at 433 K produces highly crystalline zeolites with well-defined morphologies.

The synthetic procedure and parameters described above were used to prepare a series of RA-ZSM-5-SA (SA is the Si/Al molar ratio) with varying Si/Al molar ratios (Fig. S5–S7 and Table S1, ESI†). The SEM images (Fig. S6a, ESI†) and corresponding XRD patterns (Fig. S6b, ESI†) show that all hierarchical zeolites, RA-ZSM-5-SA (SA = 12.5–100), consist of ordered rod-shaped ZSM-5 nanocrystal arrangements. Most importantly, the size of the nanorods can be controlled by regulating the Si/Al ratio. Specifically, the sizes were found to increase from *ca.* 40 nm to *ca.* 170 nm when the Si/Al ratio in the gel is changed from 12.5 to 100 (Fig. S6c, ESI†). On the other hand, when the Si/Al ratio is higher than 100 (Fig. S8, ESI†), the products are bulky crystals with smooth surfaces.

SEM and TEM images (Fig. 1a–c) of RA-ZSM-5-50 show that the hierarchical structure is composed of numerous parallelly arranged rod-shaped nanocrystals with widths of *ca.* 90 nm. The high-resolution TEM (HR-TEM) image and related fast Fourier transform (FFT) image (Fig. 1d) indicate that the nanorods are aligned along the [001] direction (*i.e.*, *c*-axis). The high-angle annular dark-field scanning transmission electron microscopy (HAADF-STEM) image and the corresponding element mapping analysis (Fig. 1e) show that Si, O, and Al elements are dispersed uniformly throughout the crystals.

Evolution time-dependent analyses were performed to gain insights into the process involved in forming RA-ZSM-5-50 (Fig. S9, ESI†). The XRD pattern (Fig. 2a) revealed that the sample recovered after 2 h is amorphous, consisting of aggregates of oligomers (Fig. S9a, ESI†). The corresponding TEM images (Fig. S10, ESI†) show that the formed particles tend to aggregate into individual zeolite crystals (about 4 μm), having local rod-shaped structures. After a longer hydrothermal reaction, crystals appear with

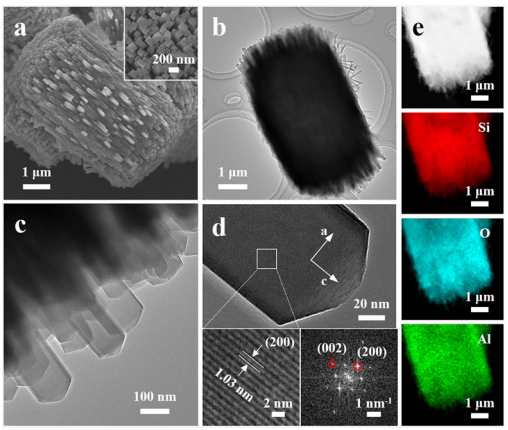

Fig. 1 (a) SEM image (inset: the side view), (b) and (c) TEM images, (d) magnified TEM image and the corresponding FFT image of an individual nanorod; (e) HAADF-TEM image of partial nanorods, and the corresponding Si, O, and Al element mapping analysis of RA-ZSM-5-50.

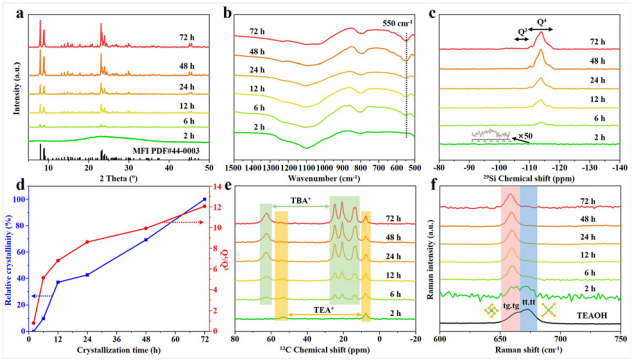

Fig. 2 (a) XRD patterns, (b) FT-IR spectra, (c) ^{29}Si MAS NMR spectra, (d) relative crystallinity (blue) and Q^4/Q^3 ratio curves (red), (e) ^{13}C MAS NMR spectra, and (f) Raman spectra of RA-ZSM-5-50 at different hydrothermal times (2–72 h).

significant numbers of small particles clustered on the surface (Fig. S9b and c, ESI†). In addition, continuous growth leads to the formation of increasing numbers of nanorod arrays, which produce unique rod-shaped crystals (Fig. S9d–f, ESI†). The band at 550 cm^{-1} in the Fourier transform infrared spectrum (Fig. 2b), assigned to the five-ring units of the MFI framework, gradually increases with time, which is consistent with the changes in crystallinity indicated by the XRD patterns.[26] This indicates that the connectivity among the five-ring units increases during the aggregation growth of zeolite.[27] We found that the growth of RA-ZSM-5-50 follows the nonclassical crystallization pathway of particle attachment.[28–30]

^{27}Al MAS NMR spectra (Fig. S11, ESI†) of the 2 h samples contain a broad signal at 55.8 ppm assignable to tetrahedral AlO_4^- units in the oligomer.[31] After increasing the hydrothermal time, the 55.8 ppm signal in the spectra gradually shifts to 54.6 ppm, and no peak at 0 ppm associated with extra-framework Al species appears. These observations demonstrate that most Al species are incorporated into the framework of MFI as tetrahedral AlO_4^-. The ^{29}Si MAS NMR spectrum (Fig. 2c and Fig. S12 and Table S3, S4, ESI†) of the 2 h samples contains two broad signals at −110.9 ppm (55%) and −112.3 ppm (45%), associated with amorphous Q^3 and Q^4 in the oligomers.[32] This indicates that only slightly ordered and crosslinked aluminosilicate oligomers enriched in silanol groups are produced during the initial crystallization. In crystal growth, a monotonically increasing trend is observed in the Q^4/Q^3 intensity ratio, which corresponds to the increase in the crystallinity of the hydrothermal product (Fig. 2d). This suggests that the Q^3 species are directly transformed into Q^4 species during crystal formation.[33] In addition, the relative content of Q^3 species decreases monotonically during crystallization (Table S4, ESI†), which was attributed to the condensation of silanol groups. It has been reported that the (001) plane of MFI intermediates has a high silanol density, which leads to a stronger interaction energy than those in the other planes.[34] Due to surface energy minimization, particle attachment preferentially occurs on the (001) plane, leading to the nanorod growth along the *c*-axis.

^{13}C MAS NMR spectra (Fig. 2e and Fig. S13a, ESI†) of uncalcined samples show that TEA^+, and not TBA^+, is present

in the sample during the early crystallization stage. It is likely associated with the preferential encapsulation of the higher charge density of TEA^+ by negatively charged aluminosilicates in forming oligomers.[35] As the hydrothermal time increases, the content of TEA^+ increases sharply to reach a plateau, after which the content of TBA^+ increases to a near constant level (Fig. S13b, ESI†). Notably, under identical conditions, TEA^+ alone fails to induce crystallization (Fig. S14a, b and e, ESI†), while TBA^+ yields single rod-shaped crystals (Fig. S2a, ESI†). Moreover, the hydrothermal reaction carried out in a two-step crystallization method, where TEA^+ and TBA^+ are added separately, results in ZSM-5 crystals but no distinct hierarchical structure (Fig. S14c, d and e, ESI†). This indicates that TBA^+ and TEA^+ need to be present simultaneously during the crystallization to form ZSM-5 zeolite and create a hierarchical structure.

Raman spectra were employed to distinguish between the two conformations of TEA^+ that are present in zeolites, which are designated as tt.tt and tg.tg, with the tg.tg conformation being predominant in ZSM-5.[36,37] Raman spectra (Fig. 2f) of uncalcined samples show that TEA^+ present in the 2 h sample consists of approximately equal amounts of tt.tt and tg.tg conformations. Then, the tg.tg conformation rapidly increases, indicating that most TEA^+ within the zeolite adopts the tg.tg conformation. It is possible that the tt.tt to tg.tg conformational transition triggers the formation of zeolites with an MFI topology, rather than MEL topology whose formation is guided by TBA^+.

The formulated crystallization mechanism for the formation of RA-ZSM-5-50 is shown in Fig. 3. At the early stage of the pathway, aluminosilicates preferentially encapsulate high-charge-density TEA^+ to form oligomers. This process is followed by oligomer aggregation, which initiates crystal formation. As the process progresses, TBA^+ becomes the predominant surface-adsorbed SDA because most of TEA^+ has been incorporated into the aggregates. Under the combined effect of the two SDAs, oligomer particles coalesce and rearrange to form crystals with rough surfaces. Due to the high interaction energy of the (001) plane, more oligomer aggregates attach to and crystallize along the *c*-axis, promoting directional growth of nanorods. Moreover, TBA^+ preferentially occupies the straight channel pores along the *b*-axis, stabilizing the *a*–*c* plane while suppressing *b*-axis growth, thereby promoting nanorod formation.[38] TEA^+ inhibits the attachment of nanoparticles on the (010) surface, which prevents coalescence to generate larger crystals.[39] This is the likely reason why nanorod sizes are governed by the Si/Al ratio and why smooth surfaces are produced when the Si/Al ratios are very high.

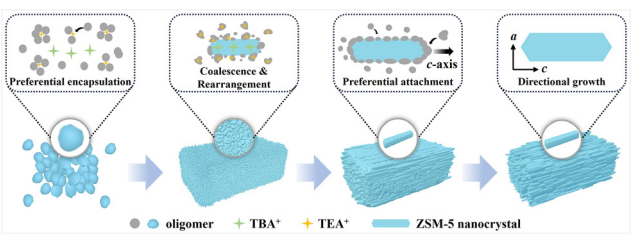

Fig. 3 Proposed mechanism of formation through a nonclassical crystallization pathway.

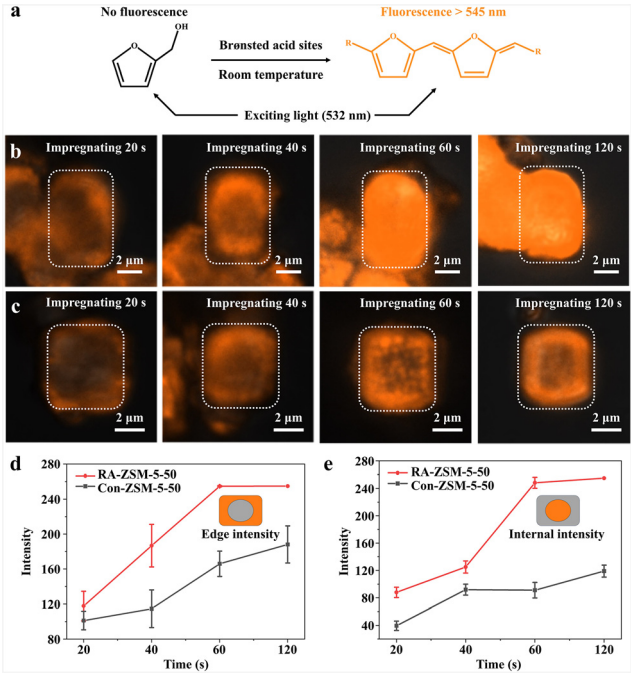

Fig. 4 (a) Schematic of the formation of the fluorescent oligomers (orange, false colors). Fluorescent images of FA oligomerization occurring in (b) RA-ZSM-5-50 and (c) Con-ZSM-5-50 at different reaction times. Plots of average fluorescence intensities *versus* time at the (d) edges and (e) interiors of the crystals of RA-ZSM-5-50 and Con-ZSM-5-50.

The fluorescent reaction (Fig. 4a–c) shows the progress of furfuryl alcohol (FA) oligomerization in RA-ZSM-5-50 and conventional ZSM-5 single crystals (Con-ZSM-5-50, Fig. S15, ESI†) at different reaction times (20, 40, 60, and 120 s). This shows that more rapid migration of fluorescence takes place in RA-ZSM-5-50 crystals compared to that in Con-ZSM-5-50 crystals. The fluorescence is rapidly generated throughout almost the entirety of the RA-ZSM-5-50 crystal after a reaction time of 60 s, while it is generated almost exclusively along the edge of Con-ZSM-5-50 (Fig. 4d, e and Fig. S16, ESI†). The results demonstrate that RA-ZSM-5-50 has superior mass transfer and crystal utilization efficiency as compared to that of Con-ZSM-5-50 because of its unique structure, which facilitates mass transfer. The methanol to olefins (MTO) reaction was used to compare the catalytic stability of RA-ZSM-5-50 zeolite and rod-shaped ZSM-11 zeolite (R-ZSM-11-50, Fig. S17, S18 and Table S2, ESI†) synthesized using a single structure-directing agent (TBAOH). Notably, RA-ZSM-5-50 zeolite has a 6 h lifetime with a methanol conversion over 99%, which is higher than the 1.3 h lifetime of R-ZSM-11-50 zeolite at a methanol conversion over 96% (Fig. S19, ESI†). To evaluate its structural stability, the rod-shaped RA-ZSM-5-50 zeolite was subjected to hydrothermal/steam treatment at 180 °C for 7 days. The results show that the morphology of this zeolite remained unchanged, indicating its excellent structural stability (Fig. S20, ESI†). Additional evidence from prolonged hydrothermal crystallization further supports this stability—after 12 days of treatment, the rod-like alignment of the RA-ZSM-5-50 zeolite remained unchanged, with no observable fusion of nanorods

(Fig. S21, ESI†). These results highlight the effectiveness of rational dual-SDA design in controlling crystallization and imparting remarkable structural stability to hierarchical zeolites.

In summary, we developed a straightforward one-step method for constructing hierarchical ZSM-5 zeolites, which utilizes TEAOH and TBAOH as SDAs to generate nanorod crystals arranged parallel to the *c*-axis. In a co-existence system of TBA^+ and TEA^+, the growth of nanorods follows a nonclassical growth mechanism of particle-attached crystallization. The size of nanorods is dependent on the Si/Al molar ratio in the range of 12.5 to 100. The ordered hierarchical structure in ZSM-5 zeolite possesses efficient mass diffusion and catalytic and structural stability. It is expected that the strategy developed in this study can be extended to other multi-SDA guided hierarchical zeolite forming processes to generate specific controllable morphologies and sizes.

We thank the Key R&D Program of Shandong Province, China (2023CXGC010314), the National Key Research and Development Program of China (2022YFB3805600, 2022YFB3805604, and 2022YFB3806800), the National Natural Science Foundation of China (22293020), the National 111 project (B20002), the Major Program (JD) of Hubei Province (2023BAA003), and the Hubei Province Key Research and Development Program (2023BAB101). We also thank the Nanostructure Research Centre for their support in collecting the S/TEM images.

Conflicts of interest

There are no conflicts to declare.

Data availability

The data supporting this article have been included in the main text and the ESI.†

Notes and references

1 C. Martínez and A. Corma, *Coord. Chem. Rev.*, 2011, **255**, 1558–1580.
2 Y. Li and J. Yu, *Chem. Rev.*, 2014, **114**, 7268–7316.
3 S. M. Wu, X. Y. Yang and C. Janiak, *Angew. Chem., Int. Ed.*, 2019, **58**, 12340–12354.
4 L. Zhang, N. Liu, C. Dai, R. Xu, G. Yu, B. Chen and N. Wang, *Chem. Synth.*, 2023, **3**, 2.
5 Y. Shen, T. T. Le, D. Fu, J. E. Schmidt, M. Filez, B. M. Weckhuysen and J. D. Rimer, *ACS Catal.*, 2018, **8**, 11042–11053.
6 E. T. C. Vogt, D. Fu and B. M. Weckhuysen, *Angew. Chem., Int. Ed.*, 2023, **62**, e202300319.
7 H. Dai, Y. F. Shen, T. M. Yang, C. Lee, D. L. Fu, A. Agarwal, T. T. Le, M. Tsapatsis, J. C. Palmer, B. M. Weckhuysen, P. J. Dauenhauer, X. D. Zou and J. D. Rimer, *Nat. Mater.*, 2020, **19**, 1074–1080.
8 R. Jain, A. Chawla, N. Linares, J. Garcia Martinez and J. D. Rimer, *Adv. Mater.*, 2021, **33**, e2100897.
9 B. J. Zeng, S. M. Wu, M. Antonietti, C. Janiak, O. Terasaki and X. Y. Yang, *Chem. Eng. J.*, 2025, **505**, 159282.
10 L. H. Chen, M. H. Sun, Z. Wang, W. Yang, Z. Xie and B. L. Su, *Chem. Rev.*, 2020, **120**, 11194–11294.
11 M. Shamzhy, M. Opanasenko, P. Concepcion and A. Martinez, *Chem. Soc. Rev.*, 2019, **48**, 1095–1149.
12 K. Ding, A. Corma, J. A. Macia-Agullo, J. G. Hu, S. Kramer, P. C. Stair and G. D. Stucky, *J. Am. Chem. Soc.*, 2015, **137**, 11238–11241.
13 S. Han, Z. Wang, L. Meng and N. Jiang, *Mater. Chem. Phys.*, 2016, **177**, 112–117.
14 Y. Ma, X. Tang, J. Hu, Y. Ma, W. Chen, Z. Liu, S. Han, C. Xu, Q. Wu, A. Zheng, L. Zhu, X. Meng and F. S. Xiao, *J. Am. Chem. Soc.*, 2022, **144**, 6270–6277.
15 H. Zhang, H. Zhang, Y. Zhao, Z. Shi, Y. Zhang and Y. Tang, *Chem. Mater.*, 2017, **29**, 9247–9255.
16 X. Niu, F. Feng, G. Yuan, X. Zhang and Q. Wang, *Nanomaterials*, 2019, **9**, 362.
17 D. Hu, H. Hu, H. Jin, P. Zhang, Y. Hu, S. Ying, X. Li, Y. Yang, J. Zhang and L. Wang, *Appl. Catal., A*, 2020, **590**, 117338.
18 Z. Qin, Z. You, K. N. Bozhilov, S. K. Kolev, W. Yang, Y. Shen, X. Jin, J. P. Gilson, S. Mintova, G. N. Vayssilov and V. Valtchev, *Chem. – Eur. J.*, 2022, **28**, e202104339.
19 Y. Xu, H. Tang, L. Liu, M. Hua, K. Chen and Y. Duan, *Chem. Eng. J.*, 2022, **450**, 138180.
20 L. F. Wang, Z. Zhang, C. Y. Yin, Z. C. Shan and F. S. Xiao, *Microporous Mesoporous Mater.*, 2010, **131**, 58–67.
21 Y. Quan, S. Li, S. Wang, Z. Li, M. Dong, Z. Qin, G. Chen, Z. Wei, W. Fan and J. Wang, *ACS Appl. Mater. Interfaces*, 2017, **9**, 14899–14910.
22 X. Zhao, S. Zeng, X. Zhang, Q. Deng, X. Li, W. Yu, K. Zhu, S. Xu, J. Liu and L. Han, *Angew. Chem., Int. Ed.*, 2021, **60**, 13959–13968.
23 W. Tai, W. Dai, G. Wu and L. Li, *Chem. Synth.*, 2023, **3**, 38.
24 O. Veselý, M. Shamzhy, W. J. Roth, R. E. Morris and J. Čejka, *Cryst. Growth Des.*, 2024, **24**, 2406–2414.
25 B. J. Zeng, S. M. Wu, M. B. Gao, G. Tian, L. Y. Wang, Z. W. Yin, Z. Y. Hu, W. Zhang, G. G. Chang, M. Ye, C. Janiak, O. Terasaki and X. Y. Yang, *J. Am. Chem. Soc.*, 2024, **146**, 33423–33433.
26 G. Coudurier, C. Naccache and J. C. Vedrine, *J. Chem. Soc.*, 1982, **24**, 1413–1415.
27 D. Lesthaeghe, P. Vansteenkiste, T. Verstraelen, A. Ghysels, C. E. A. Kirschhock, J. A. Martens, V. V. Speybroeck and M. Waroquier, *J. Phys. Chem. C*, 2008, **112**, 9186–9191.
28 A. I. Lupulescu and J. D. Rimer, *Science*, 2014, **344**, 729–732.
29 J. J. De Yoreo, P. U. Gilbert, N. A. Sommerdijk, R. L. Penn, S. Whitelam, D. Joester, H. Zhang, J. D. Rimer, A. Navrotsky, J. F. Banfield, A. F. Wallace, F. M. Michel, F. C. Meldrum, H. Colfen and P. M. Dove, *Science*, 2015, **349**, aaa6760.
30 H. Li, J. Yu, K. Du, W. Li, L. Ding, W. Chen, S. Xie, Y. Zhang and Y. Tang, *Angew. Chem., Int. Ed.*, 2024, **63**, e202405092.
31 S. Wang, L. Zhang, S. Li, Z. Qin, D. Shi, S. He, K. Yuan, P. Wang, T.-S. Zhao, S. Fan, M. Dong, J. Li, W. Fan and J. Wang, *J. Catal.*, 2019, **377**, 81–97.
32 J. K. Reddy, K. Motokura, T.-R. Koyama, A. Miyaji and T. Baba, *J. Catal.*, 2012, **289**, 53–61.
33 Z. Sheng, H. Li, K. Du, L. Gao, J. Ju, Y. Zhang and Y. Tang, *Angew. Chem., Int. Ed.*, 2021, **60**, 13444–13451.
34 Q. Zhang, J. Li, X. Wang, G. He, L. Li, J. Xu, D. Mei, O. Terasaki and J. Yu, *J. Am. Chem. Soc.*, 2023, **145**, 21231–21241.
35 O. A. Fouad, R. M. Mohamed, M. S. Hassan and I. A. Ibrahim, *Catal. Today*, 2006, **116**, 82–87.
36 T. Ikuno, W. Chaikittisilp, Z. Liu, T. Iida, Y. Yanaba, T. Yoshikawa, S. Kohara, T. Wakihara and T. Okubo, *J. Am. Chem. Soc.*, 2015, **137**, 14533–14544.
37 J. E. Schmidt, D. Fu, M. W. Deem and B. M. Weckhuysen, *Angew. Chem., Int. Ed.*, 2016, **55**, 16044–16048.
38 C. E. A. Kirschhock, R. Ravishankar, L. V. Looveren, P. A. Jacobs and J. A. Martens, *J. Phys. Chem. B*, 1999, **103**, 4972–4978.
39 M. K. Choudhary, M. Kumar and J. D. Rimer, *Angew. Chem., Int. Ed.*, 2019, **58**, 15712–15716.